# A SELF-ACTING THRUST BEARING FOR HIGH SPEED MICRO-ROTORS

**C. W. Wong, X. Zhang†, S. A. Jacobson, and A. H. Epstein**

Gas Turbine Laboratory, Massachusetts Institute of Technology, Cambridge, MA 02139, USA
†Department of Manufacturing Engineering and Fraunhofer USA Center for Manufacturing Innovation, Boston University, Boston, MA 02215, USA

## ABSTRACT

A self-pressurizing hydrodynamic thrust bearing has been designed, fabricated and tested up to speeds of 450,000 rpm on a 4.2 mm diameter MEMS radial inflow turbine. This test device demonstrated the load bearing capability predicted by the macro-scale gas bearing theory derived from the literature. The design of the devices tested was compromised to fit an existing geometry and fabrication sequence. Given more design freedom, these bearings should be capable of operating at several million rpm. Compared to existing hydrostatic thrust bearings, a hydrodynamic approach offers significantly simplified fabrication and elimination of the need for a source of pressurized gas external to the bearing.

## INTRODUCTION

Rotating micromachinery must spin at high rotating speed to achieve high power density and these high rotating speeds require low friction bearings for long life and low drag. Work has been reported on MEMS compressors, turbines, motors, generators, pumps and gas turbine engines [1]. A 4 mm rotor diameter turbine spinning on hydrostatic gas bearings at 1.4Mrpm was previously reported [2,3]. This device consists of a 4 mm diameter by 500 μm thick rotor with radial turbine blades on one side (the other side may consist of an electric motor or generator). A journal bearing on the disk rim supports the radial loads while thrust bearings at on the either side of the center line support axial loads. The entire device (herein referred to as a "microbearing rig"), consisting of the rotor, bearings, and associated plumbing, is constructed from five DRIE'd silicon wafers precision aligned and diffusion bonded in to a stack.

In the previous microbearing rigs the thrust bearings have been of hydrostatic design, that is the gas film supporting the rotor is supplied through metering orifices from a source external to the bearing (and perhaps the device). While this approach has been shown to work well and has great experimental flexibility, simplicity is often a virtue in microfabrication. Specifically for the devices reported to date, hydrostatic thrust bearings have two disadvantages: (1) an air source external to the bearing is needed (typically at 2-5 atm), and (2) fabrication complexity (2 of the 5 wafers required for the turbine are needed for the thrust bearing plumbing). Hydrodynamic thrust bearings offer an alternative approach. In these bearings, the gas film pressure is generated within the bearing by the relative motion of the rotor. This eliminates the need for an external gas supply and, in this device, eliminates 2 of the 5 wafers. This paper presents the design, fabrication of and experiments on hydrodynamic self-acting thrust bearings.

## CONCEPTS AND DESIGN

This study was constrained by the requirements that that the hydrodynamic bearings must fit within the current device geometry and be compatible with the existing fabrication sequence. Also, the hydrodynamic bearings must support the same static and dynamic loads as the hydrostatic bearings and remain stable within the device operating envelop. The rotor in Figure 1 is a planar, radial inflow turbine with a 4.2 mm rotor diameter and 225 μm span airfoils. A 400 μm diameter thrust bearing pad is located at the rotor center on the forward (airfoil) side. This thrust pad rotates relative to a stationary thrust bearing surface of similar diameter. In the hydrostatic thrust bearing, the stationary bearing surface is perforated with a circular array of 10 μm diameter nozzle orifices fed from a plenum which supplies the gas lubricating film between the bearing surfaces. Typically a flow of 10 sccm at 2-5 atm is needed to provide sufficient load capacity and axial stiffness.

Hydrodynamic bearings use viscous drag (often enhanced with shallow spiral grooves) to generate a pressure gradient in the bearing which increases toward the rotor center. This pressurized gas film provides the bearing load capacity and stiffness.

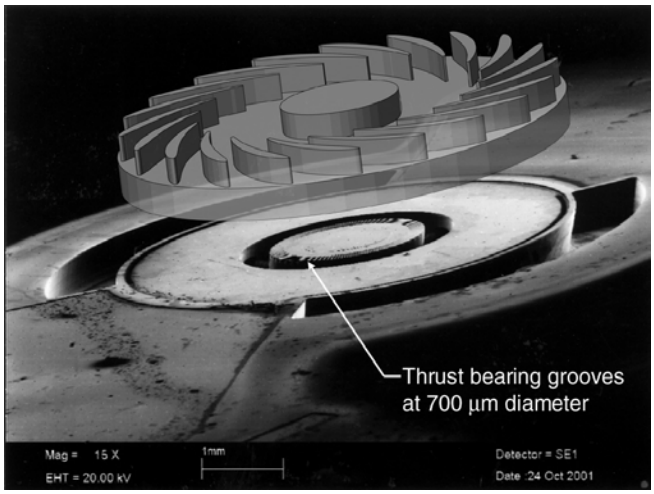


***Figure 1.*** *SEM image of a hydrodynamic thrust bearing with a superimposed 4.2 mm dia microturbine. Viscous drag associated with the rotation of the turbine generates a radial pressure gradient in the spiral grooves located on the inner thrust bearing structure.*

Many hydrodynamic design variants are reported in the macro-scale thrust bearing literature [5,6]. The planar spiral groove bearing appeared attractive in term of fabrication ease. A full profile of the spiral groove bearing was chosen

to maximize the load capacity and stiffness. Referring to the nomenclature in Figure 2, the load capacity $L_t$ and drag $D_t$ of a full flat spiral groove bearing can be expressed in terms of geometrical parameters following Muijderman [7]:

$$L_t = \frac{3\pi\mu\omega\, r_2^4}{2h_2^2}(1-\lambda^4)\, g_1(\alpha,H,\gamma)\, C_2(\alpha,H,\gamma,\lambda,\kappa) \quad (1)$$

$$D_t = \frac{\pi\mu\omega^2\, r_2^4}{2h_2}(1-\lambda^4)\, g_2(\alpha,H,\gamma) \quad (2)$$

where $\mu$ is the fluid viscosity, $\omega$ the angular velocity in rad/s, $\lambda$ the ratio of the inner radius $r_1$ to the outer radius $r_2$ as shown in Figure 2, $\alpha$ the spiral groove angle, $\gamma$ the ridge width to groove width ratio, $\kappa$ the number of grooves, $h_2$ the bearing film height above the ridges, $H$ the ratio of $h_2$ to the bearing film height above the grooves, $g_1$ and $g_2$ analytical terms from a simplified linear pressure profile in the grooves, and $C_2$ a groove-end effect correction factor.

Equations 1 and 2 show that the load capacity and bearing stiffness are dependent on the turbine rotational speed. Using equation (1), we optimized the design for the maximum load capacity $L_t$ by varying the geometry, under constraint of bearing dynamic stability [8]. Dynamic stability can be considered in terms of a compressibility number $\Lambda_c$ where

$$\Lambda_c = \frac{3\mu\omega\, r_2^2}{p_a h_2^2} \quad (3)$$

with $p_a$ as the ambient pressure, such that $\Lambda_c$ must be less than a critical compressibility number obtained via a small perturbation analysis or a simplified analytical approach for a given geometry.

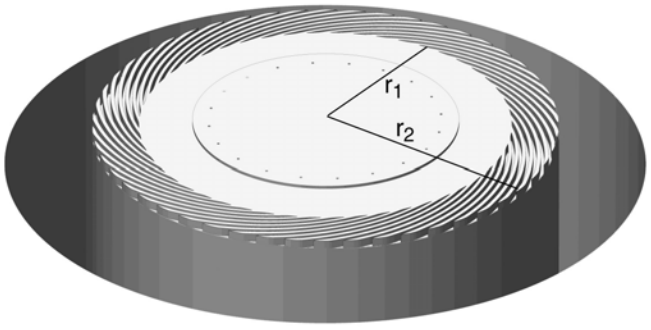


***Figure 2.*** *Model of a full planar spiral groove bearing, depicting the geometric parameters.*

The resultant design has a ridge depth of 1.0 µm, a groove angle of 16 degrees, and $r_1$ and $r_2$ of 560 and 700 µm, respectively. Figure 3 shows the calculated rotor net load bearing capacity (the gross force each bearing can sustain minus the force applied by the opposing bearing) for a matched pair of opposing hydrodynamic thrust bearings as a function of axial eccentricity and rotational speed (eccentricity is the axial position of the rotor normalized by the total thrust bearing gap). This optimized load capacity ranges from +0.34 to –0.34N. For this geometry, the analysis predicts a dynamic stability boundary of 820,000 rpm.

Hydrodynamic bearing stiffness increases linearly with rotational speed, reaching $6 \times 10^5$ N/m at 820,000 rpm. In contrast, the stiffness of the hydrostatic bearing is $3 \times 10^5$ N/m and is independent of speed. The drag of the hydrodynamic bearing, equation (2), increases quadratically with speed, reaching 0.05 W at 820,000 rpm, while that of the hydrostatic bearing is 0.03 W. One hydrodynamic thrust bearing accounts for about 10% of the total bearing system drag (journal plus thrust bearings).

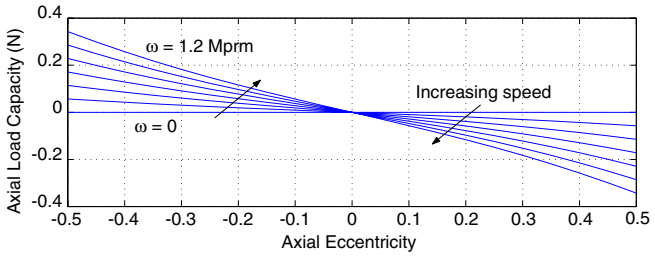


***Figure 3.*** *Optimized net bearing load capacity as a function of axial eccentricity and rotational speed. This is the net rotor load capacity for a matched pair of opposing hydrodynamic thrust bearings.*

## FABRICATION DEVELOPMENT

The fabrication process was modified from that first reported by Lin *et al* [4]. A five silicon wafer fusion-bonded stack was microfabricated with a series of DRIE and RIE sequences to create the fluid flow channels and the enclosed microturbine and bearings. Only the aft thrust bearing wafer-levels were modified to include the hydrodynamic, hybrid hydrodynamic-hydrostatic and hydrostatic bearing designs.

Comprising of four RIE and two DRIE steps, the first and second RIE etch depths define the hydrodynamic and hydrostatic stiffness respectively and their depth must be closely controlled (to ± 0.1 µm). The third RIE etch creates the spiral grooves, while fourth etch produces the relatively large gap, 8 µm between the aft-side of the rotating microturbine and the adjacent stationary surface, to reduce viscous drag losses on the aft side of the rotor. Note that if a solely hydrodynamic bearing wafer was produced, the process flow can be reduced to two thrust bearing RIE steps.

An SEM of a hybrid thrust bearing is presented in Figure 4. The hydrodynamic spiral grooves are shaped according to the optimized design discussed previously. The hydrostatic thrust bearing orifices, positioned inward of the spiral grooves, are placed on a raised platform to provide

sufficient hydrostatic stiffness at startup. To produce the required hydrostatic stiffness, the orifice diameter must be controlled to ± 0.5 µm.

The completed thrust bearing wafers are thermally fusion-bonded with a rotor wafer sandwiched between them, and two additional wafers added on the outside to provide gas piping to the bearings and turbine inlet. The microbearing device wafer is then die-sawed and packaged for testing.

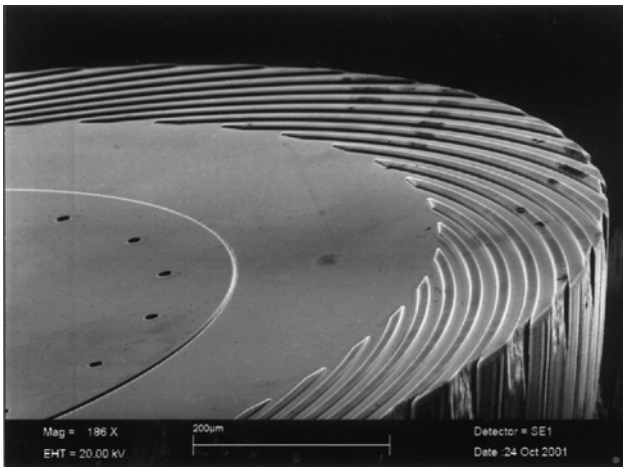


***Figure 4. .*** *A microfabricated hybrid hydrodynamic-hydrostatic thrust bearing. The orifice diameter is 10 µm and the groove depth is 2.2 µm.*

## Experimental Description

The microbearing device was tested in a package developed by Lin *et al* [4] and Fréchette *et al* [3]. Pressure taps and mass flow meters are used to measure the fluid flow. An external 100 µm diameter fiberoptic speed sensor measured the rotational speed. For these tests, the journal bearing was operated with an externally supplied flow (i.e. in hydrostatic mode). The journal pressure was varied with rotational speed to provide the stiffness needed for stable operation.

We will first discuss tests of a device with a hybrid aft-side thrust bearing. The device as fabricated had a spiral groove depth of 1.53µm rather than the 1.0 µm design value, lowering the predicted onset of instability speed to 600,000 rpm. The bearing flow rate verses axial position was calibrated by manipulating the forward and aft thrust bearing flows to move a stationary rotor fore and aft. After calibrating the device, a series of tests were conducted in which the forward and aft hydrostatic flows were stabilized first (suspending the rotor) and then the turbine drive air started to spin the rotor. After the rotor speed was stabilized, the aft bearing pressure was vented to ambient so that the load capacity of the aft bearing was dependent only on the hydrodynamic action of the spiral grooves. At speeds below 100,000 rpm, the rotor stopped when the aft hydrostatic bearing air was turned off, showing that the hydrodynamic load capacity at these speeds was less than that required to support the aft rotor forces (the sum of the forward thrust bearing load and loads resulting from the pressure differences across the rotor disk). At rotational speeds above 169,000rpm, the turbine continued to operate when the aft air supply was stopped, demonstrating that at these speeds the hydrodynamic forces alone were sufficient to support the rotor. This particular device operated stably up to 450,000 rpm, at which point the rotor "crashed".

By varying the forward thrust bearing pressure and monitoring the resultant flow rate at various speeds, we estimated the load capacity of the hybrid bearing. This experimentally derived gross load capacity of the hydrodynamic bearing is compared with predictions in Figure 5. The dotted lines are model predictions at different axial eccentricities. The measured load capacity is shown as data points with a least-squares fit solid line. The dashed line is the capacity predicted by the model at the measured eccentricity (0.27). The measured load capacity is about 50% greater than the predicted value, but both show the same trend with speed. Note that the experimental uncertainties associated with these measurements are relatively large (as shown by the error bars).

A second, purely hydrodynamic device (no orifices in the aft bearing) was tested. Figure 6 shows a speed history with the device reaching 100,000 rpm. (The instabilities at 30,000 to 40,000 rpm reflect the journal bearing natural frequency.) This device reached 233,000rpm before crashing. Post test analysis suggest that the crash may have been due to a mismatch between the forward and aft thrust bearings, as the forward hydrostatic thrust bearing leaked and therefore provided a reduced load capacity.

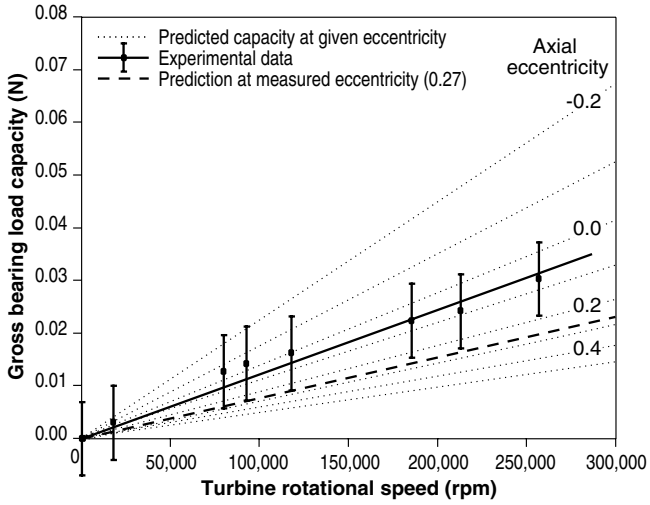


***Figure 5.*** *A comparison of experimentally derived and model predicted gross load capacity for a hybrid thrust bearing operated in hydrodynamic mode.*

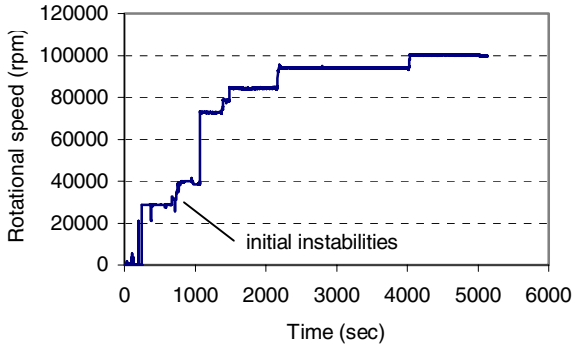


***Figure 6.*** *Time history of a device with a hydrodynamic aft thrust bearing.*

## CONCLUSIONS

A self-pressurizing hydrodynamic thrust bearing was designed, fabricated and tested up to speeds of 450,000 rpm on a 4.2 mm diameter MEMS radial inflow turbine. This test device demonstrated the load bearing capability predicted by the macro-scale gas bearing theory in the literature.

Further experimental work is needed to better characterize the operation of these devices at higher speeds, including stability, load capacity, and dissipation. Also, many start-stop cycles are needed to assess the bearing lifetime, which is presumably limited by the tribology of the surface rubbing prior to liftoff.

The design of the devices tested was compromised to fit an existing geometry and fabrication sequence. Given more design freedom, these bearing should be capable of operating at several million rpm. Compared to existing hydrostatic thrust bearings, a hydrodynamic approach offers significantly simplified fabrication and elimination of the need for a source of pressurized gas external to the bearing.

## ACKNOWLEDGEMENTS

This effort built on the work of C. C. Lin and L. G. Fréchette in device fabrication and testing. The authors would like to thank K. S. Breuer for his contributions to the modeling. The advice of M. A. Schmidt, J. G. Brisson and F. F. Ehrich was invaluable. L. Ho contributed to the device fabrication. This work was supported by the Army Research Office and DARPA, managed by Dr. T. Doligalski and Dr. R. Rosenfeld respectively.

## REFERENCES

[1] A. H. Epstein *et al.*, Plenary Lecture, 8th International Symposium on Transport Phenomena & Dynamics of Rotating (ISROMAC-8), Honolulu, HI, March 2000.

[2] C. W. Wong, *Design, Fabrication, Experimentation and Analysis of High-Speed Microscale Gas Bearings*, Masters of Science thesis, Massachusetts Institute of Technology, 2001.

[3] L. G. Fréchette *et al*., Hilton Head Solid-State Sensor & Actuator Workshop, Hilton Head, SC, June 2000, pp. 43-47.

[4] C.C. Lin *et al.*, 12th IEEE International Conference on MEMS, Orlando, FL, January 1999, pp. 529-533.

[5] B. J. Hamrock, *Fundamentals of Fluid Film Lubrication*, McGraw-Hill series in Mechanical Engineering, McGraw-Hill, New York, New York, 1st edition, 1994, pp. 329-349.

[6] Mechanical Technology Incorporated, *Design of Gas Bearings*, Mechanical Technology Incorporated, Latham, New York, 1986, pp. 6.3.2-6.3.16.

[7] E. A. Muijderman, *Spiral Groove Bearings*, Philips Technical Library, N.V. Philips' Gloeilampenfabrieken, Eindhoven, The Netherlands, 1st edition, 1966, pp. 59-116.

[8] V. N. Constantinescu and S. Galetuse, *Stability Criterion for spiral groove thrust gas bearings*, Journal of Tribology: Transaction of ASME, October 1990, pp. 112:734-737.

[9] J. L. Kerrebrock, *Aircraft Engines and gas turbines*, The MIT Press, Cambridge, Massachusetts, 2nd edition, 1992, pp. 392-394.